

Dynamic Stress Triggering during the Great 25 March 1998 Antarctic Plate Earthquake

by Andrea Antonioli, M. Cocco, S. Das, and C. Henry

Abstract We investigate the coseismic stress redistribution during the 25 March 1998 great Antarctic plate (M_w 8.1) earthquake, in which the mainshock consisted of two distinct subevents separated in time by several tens of seconds. We compute the dynamic stress time histories for the fault geometry and the rupture and slip history determined by Henry *et al.* (2000), using the discrete wavenumber and reflectivity method of Cotton and Coutant (1997), both for a homogeneous and a stratified half-space. We first image the coseismic stress evolution caused by the first subevent on the fault plane of the second one for both the velocity models. We compute both shear and normal stress changes and a time-dependent Coulomb failure function (CFF). Our results show that the shear stress changes have larger amplitudes than the other stress components and hence are the primary control on the evolution of the CFF. The dynamic stress amplitudes are larger than the static stress perturbations, with the largest positive dynamic stress peak on the second subevent fault plane reaching slightly less than 0.2 MPa at 60 sec and 65 sec after the nucleation, for the layered and the homogeneous crustal models, respectively. We suggest that the dynamic stress changes caused by the first subevent promoted a nearly instantaneous failure on the second subevent fault.

Introduction

Different investigations have shown that faults interact dynamically with one another (see Das and Aki, 1977; Harris and Day, 1993; and Harris, 1998, and references therein) and that faulting can be triggered due to dynamic stress changes (Gomberg *et al.*, 1997, 1998; Belardinelli *et al.*, 1999). The fact that static stress changes can also promote failures was suggested by Rybicki (1973) using a dislocation faulting model and later by Das and Scholz (1981) using a 2D crack model. Since then many investigations have focused on both static and dynamic triggering (see Harris, 1998; King and Cocco, 2000, and references therein), and the attention was concentrated in finding constraints and observational tests. We point out that in the near field, permanent and transient stress changes cannot be separated, but long-range interactions are dominated by dynamic stress changes associated with the passing of seismic waves (Hill *et al.*, 1993; Gomberg *et al.*, 1997). In this article, we consider an earthquake that provides examples of both static and dynamic stress perturbations. The 25 March 1998 Antarctic Plate earthquake was the largest intraplate event ever recorded and the largest strike-slip event since 1977. Its magnitude (M_w 8.1) together with the relatively low rate of seismic activity of the plate make it very interesting for the study of stress transfer. The epicenter (62.88° , 149.53°) (National Earthquake Information Center) is 250 km from the

Antarctic–Australia plate boundary and about 100 km from the nearest earthquake (M_w 5.6, 1981) reported by the Harvard CMT catalog (Fig. 1). The stress regime in the mainshock region is rotated by 90° from that at the plate boundary, leading us to consider this left-lateral strike-slip event as being isolated from the plate-boundary stresses.

Several investigations have focused on the rupture process of this earthquake (Nettles *et al.*, 1999; Antolik *et al.*, 2000; Henry *et al.*, 2000) and have led to different source models. Nettles *et al.* (1999) did not provide a full rupture history. Antolik *et al.* (2000) proposed a composite rupture consisting of separate normal and strike-slip ruptures, which in combination have a large non-double-couple component. They reject a pure double-couple mechanism on the basis of poor fits to body-wave data obtained using the nodal plane of the Harvard CMT solution. Henry *et al.* (2000) showed that the mantle-wave data can be fitted without the non-double-couple component and that for this earthquake the best double-couple solution does not correspond to a true optimal solution. Since the model of Henry *et al.* (2000) fits both body- and mantle-wave data better than the more complicated rupture process of Antolik *et al.* (2000) without invoking a non-double-couple component, we use the former in this article. The moment rate functions found in all three studies cited previously are similar, showing that the earth-

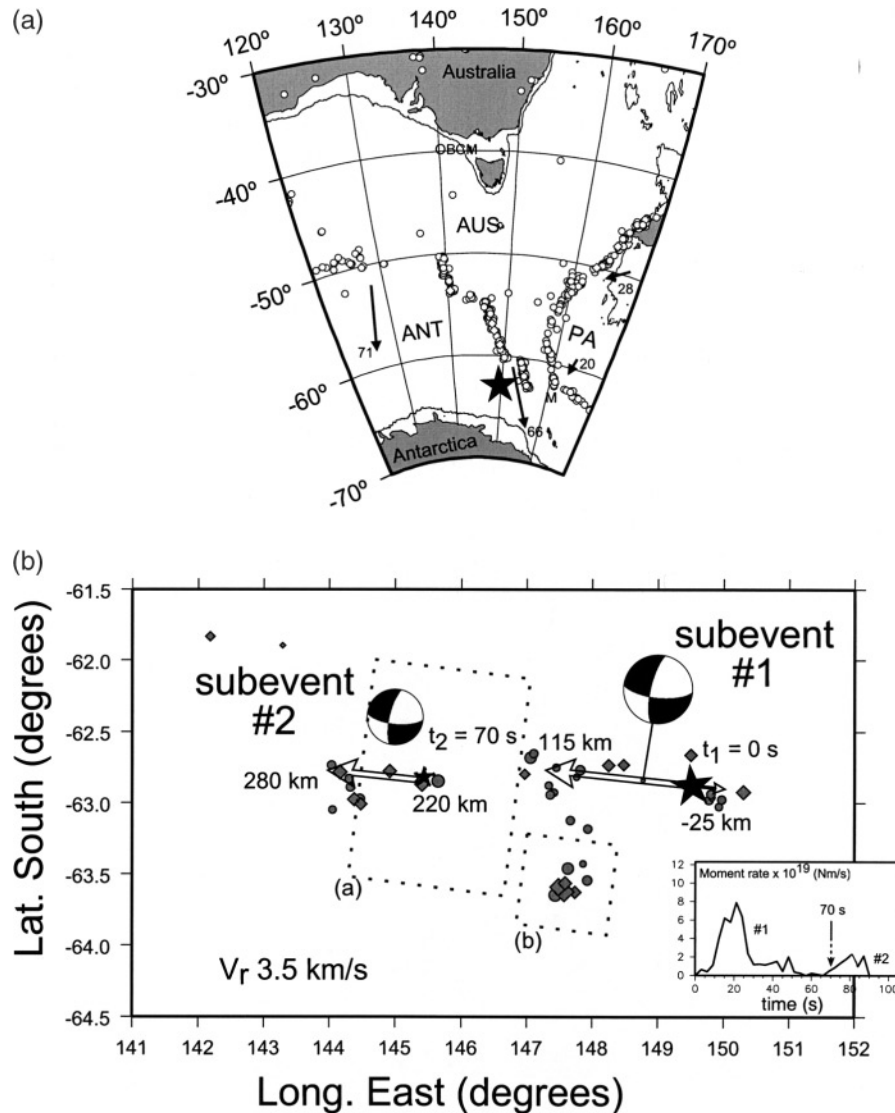


Figure 1. (a) (from Henry *et al.*, 2000). Region of the Antarctic plate earthquake, with the main events ($m_b > 5$) of the period 1 January 1964–31 July 1997 (circles) and of the period 1 August 1997–24 March 1998 (diamonds). The dark star shows the epicenter of the 1998 M_w 8.0 event. (b) Main features of the mainshock. Arrows show location and directivity of the two subevents. Times and distances are referred to the first subevent nucleation point. Boxes a and b indicate the two regions in which we calculated the stress maps. In the box the moment rate function is shown.

quake consisted of two subevents, the second one initiating roughly 70 sec after the first.

The relatively short time separation of tens of seconds between the two subevents and the distance between their epicenters (see Fig. 1b) imply small static stress changes. Therefore, it is particularly relevant to evaluate the time-dependent stress perturbation on the second subevent fault plane to find some evidence of dynamic fault interaction. Toda and Stein (2000) have investigated the correlation between the aftershocks and the cumulative stress changes caused by this composite event by analyzing the static stress changes in a homogeneous half-space (Okada, 1992; King *et al.*, 1994). They calculated the induced stress perturbation

adopting the different source models proposed in the literature. Their results show that a good correlation with the aftershock locations can be found for most of the source models: 60% to 94% of the aftershocks were located in the regions of static stress increase caused by the main event. In the present study we are interested in computing the dynamic stress evolution to understand the role played by the transient stress changes in promoting the second subevent rupture.

Methodology

We compute the dynamic stress evolution caused by an extended shear rupture by means of the reflectivity method

(Kennet and Kerry, 1979) and the discrete wavenumber decomposition (Bouchon, 1981) as originally proposed by Cotton and Coutant (1997). This method allows us to describe the transient (dynamic) and the permanent (static) stress changes outside a rupturing fault embedded in a horizontally stratified half-space with cylindrical symmetry. We assign the distribution of slip on a rupturing fault discretized by a set of point sources, on which we specify the source time function and the rupture velocity (see also Belardinelli *et al.*, 1999). We calculate the six components of the stress tensor and the Coulomb failure function (CFF) on a set of receiver points located outside the master fault, which can be resolved on a secondary plane described by its rake, strike, and dip angles. This procedure allows using a nonuniform slip distribution on the master fault plane as well as computation of Green's functions for a layered model in which P - and S -wave velocities, density, and anelastic attenuation parameters (Q_p and Q_s) are assigned in each layer. Therefore, the proposed methodology includes the effects of the stratification, allowing more general applications with respect to most of the elastostatic solutions, which are calculated in a homogeneous half-space. The time-dependent Coulomb failure function is computed, according to its definition, at a generic point \bar{y} outside the master fault as

$$\Delta\text{CFF}(\bar{y}, t) = \Delta\tau(\bar{y}, t) + \mu' \cdot \Delta\sigma(\bar{y}, t), \quad (1)$$

where $\mu' = \mu(1 - B)$ is the effective friction coefficient, μ is the coefficient of friction, and B is the Skempton parameter (Simpson and Reasenberg, 1994; Stein *et al.*, 1992). $\Delta\tau$ is the shear stress, and $\Delta\sigma$ is the normal stress changes, and the latter is assumed positive for extension. In all the following applications we use a value of 0.4 for μ' (see King and Cocco, 2000). We compute shear, normal, and Coulomb stress changes either on the second subevent fault plane or on horizontal maps located outside the master fault at a depth of 8 km as indicated by the dotted boxes shown in Figure 1b. The common interpretation is that positive values of the ΔCFF promote failures (see Harris, 1998; Stein, 1999; King and Cocco, 2000), and this is generally believed to be true both for static and dynamic stress changes. However, the application of negative static or dynamic stress perturbations seems to produce different effects. In fact, while negative static stress changes tend to inhibit or delay the occurrence of induced events, negative transient stress does not produce any effect (Gomberg *et al.*, 1998; Belardinelli *et al.*, 2000).

Rupture History and Velocity Model

We use the source model for the two subevents proposed by Henry *et al.* (2000) who analyze broadband body and mantle waves. The moment rate release shows two distinct episodes (see Fig. 1b), the second one lasted from 70 to 90 sec after the onset of the first rupture, indicating that the mainshock is a double event. The fault-plane solution for the first rupture episode shows a strike angle of 96° , dip

69° , and rake -18° . We consider a simple rupture history consisting of a Haskell model with constant rupture velocity of 3.5 km/sec and the nonuniform slip distribution proposed by Henry *et al.* (2000). The best estimate of total seismic moment is 1.2×10^{21} N m, and the estimated rupture velocity ranges between 3 and 4 km/sec. The region of high moment release extends 115 km west and 25 km east of the epicenter along the strike direction. The best-fitting solution suggests that there is little moment release below 15-km depth. Considering a maximum depth of 15 km and a length of 140 km yields a static stress drop of 240 bars. The second subevent fault parameters are less well constrained: its fault plane begins 220 km west of the epicenter and is roughly 60 km long (see Fig. 1b). We use the same strike, dip, and rake angles for both subevents and a fault width of 20 km extending from the Earth surface following Henry *et al.* (2000). We assign the distribution of slip on the main fault, discretized by a set of 24 squared subfault (10×10 km²) and compute the stress evolution on a series of receivers placed on the subevent fault plane and on two regions surrounding the main fault (shown in Fig. 1b). Unfortunately the crustal structure in the earthquake region is not well known. We have computed the stress time histories using both a homogeneous and the same stratified crustal structure used by Henry *et al.* (2000) and taken from Mooney *et al.* (1998) (Table 1).

Modeling Results

We have computed the six components of the induced stress tensor (σ_{ij}) from which we calculated the normal, shear, and Coulomb stress changes caused by the first subevent on the second subevent fault plane. In Figure 2 we compare the time histories of the induced Coulomb stress calculated on receivers located on the second subevent fault plane at the eastern edge, 220 km west of the main epicenter (see the sketch in Fig. 2) and at different depths, for the two velocity models listed in Table 1. As expected the stress time histories calculated from the homogeneous model do not change with the receiver depth. Timing of dynamic stress peaks depends on the crustal velocity model. For the homogeneous case, the first positive peak is 0.093 MPa and arrives about 37 sec from the onset of first rupture, whereas the second positive peak of 0.15 MPa is reached after about

Table 1
Adopted Velocity Models

	V_p (km/sec)	V_s (km/sec)	ρ Mg/m ³	d (km)
Layered Medium				
Sediment	1.90	0.80	1.90	0.5
Basement	6.40	3.40	2.90	6.5
Mantle	8.15	4.65	3.35	–
Homogeneous Medium				
Crust	7.00	4.00	3.00	–

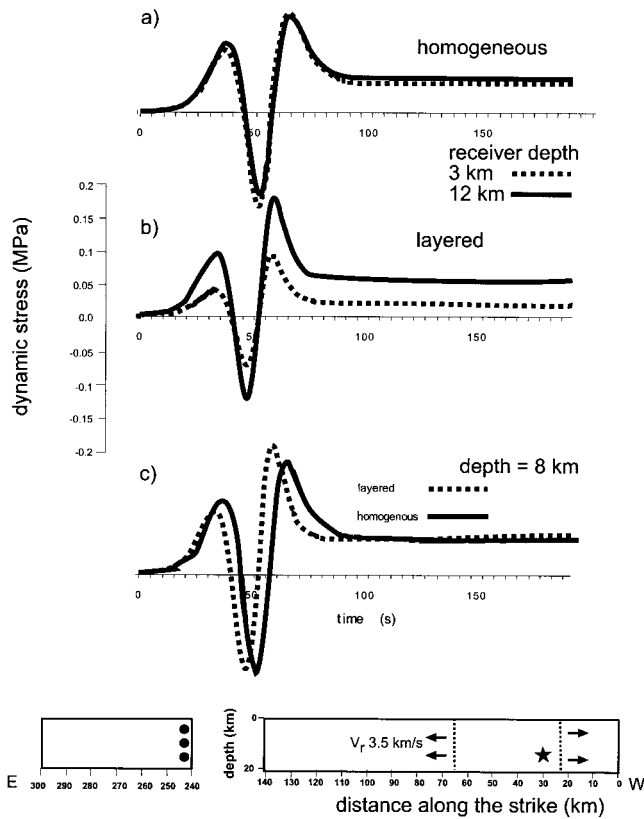


Figure 2. Time histories of Coulomb stress computed for the velocity models listed in Table 1 at different depths, at the eastern edge of the second subevent fault, as shown in the sketch at the bottom of the figure. The dots show the points in which the computations were performed.

65 sec. The negative stress peak is -0.138 MPa at 52 sec. On the contrary, in the layered model the deeper receivers show larger dynamic stress amplitudes than the shallower ones. For the shallow receiver the second positive peak has a value of 0.083 MPa at a time of 59 sec, whereas it is 0.161 MPa for the deep receiver (solid line). The static stress value does not considerably change with the assumed crustal model, and it is smaller (0.045 MPa) than dynamic stress amplitudes; it is reached after nearly 100 sec. The difference between the arrival times of the dynamic stress peaks for the two velocity structures here considered is of the order of 5–8 sec (Fig. 2c).

In Figure 3 we compare the shear, normal, and Coulomb stress changes calculated at the grid point located at 8.0 -km depth and for the two velocity models considered in Figure 2. Figure 3 clearly shows that the normal stress changes are much smaller than the induced shear stress. For this reason, the latter represent the dominant contribution to the Coulomb stress perturbation. This result does not depend on the adopted velocity structure. This implies that the calculated Coulomb stress changes are not sensitive to the adopted value of the effective friction coefficient used in equation (1).

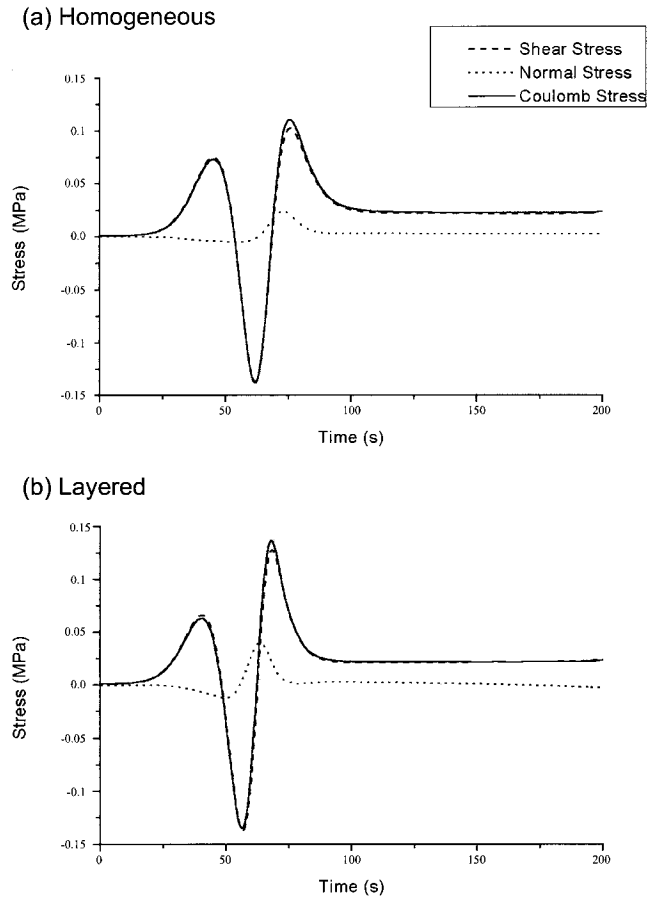


Figure 3. Comparison between shear, normal, and Coulomb stress changes calculated at a grid point located on the eastern edge of the second subevent fault at 8 -km depth and for the velocity models listed in Table 1 (as shown in Fig. 2). (a) Homogeneous model; (b) layered model.

In order to investigate the spatiotemporal evolution of the induced stress field we image the Coulomb stress changes both on a map (which coincides with the horizontal layer indicated by box a in Fig. 1b and located at 8 -km depth) and on the assumed fault plane. Figure 4 shows different snapshots (every 10 sec) of Coulomb stress changes on this layer at 8 -km depth. This figure shows that the largest amplitudes of Coulomb stress changes in the area of the second subevent are reached after 60 sec for the stratified model and 70 sec for the homogeneous one. The second subevent is located about 220 km west from the first subevent nucleation point along its strike direction, and the similarity between the two fault-plane solutions explains the observed increase of Coulomb stress. This is more evident analyzing the Coulomb stress evolution on vertical sections: Figure 5 displays the snapshots of stress changes every 10 sec on the second subevent fault plane. It is evident that the increase of Coulomb stress within the first 30 sec is followed by a sharp decrease due to the passage of the negative stress pulse. In the layered model this is more concentrated at depths rang-

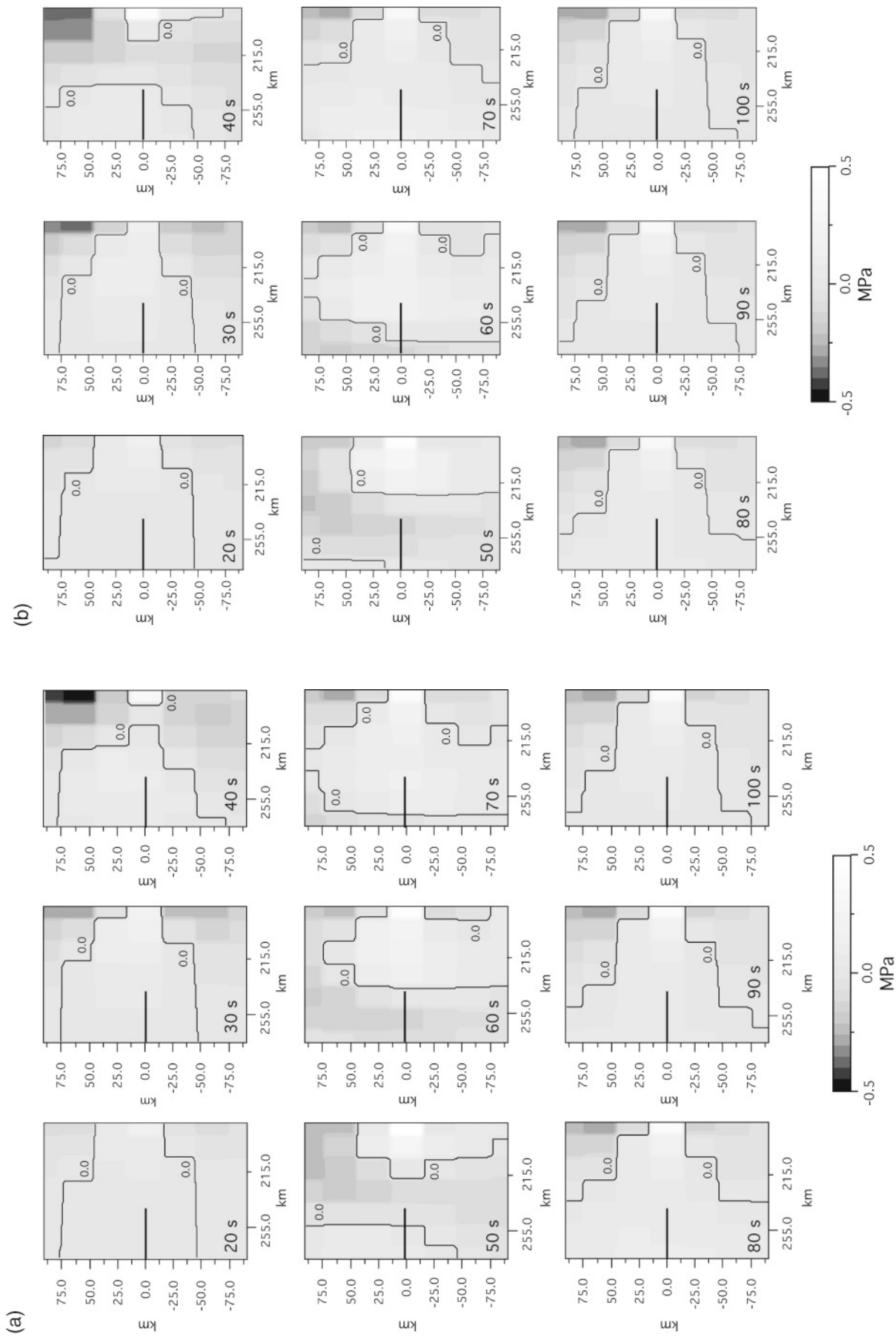


Figure 4. Map view of Coulomb stress changes calculated every 10 sec (from 20 to 100 sec) around the second subevent fault (see box a in Fig. 1) for different velocity models (shown in Table 1). The solid line inside the box indicates the position of the second subevent fault. (a) Homogeneous model; (b) layered model.

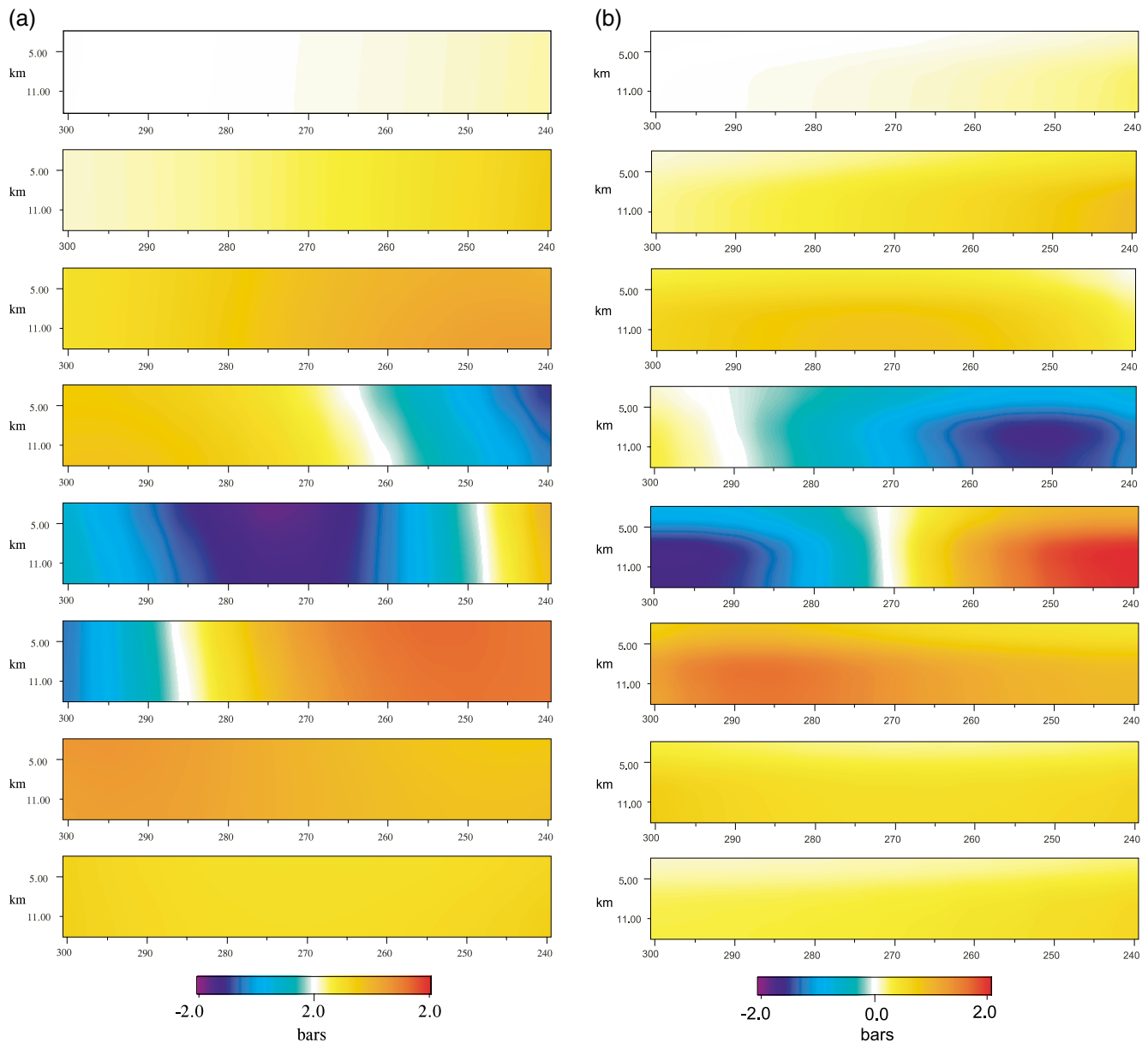


Figure 5. Snapshots of Coulomb stress changes on the fault plane that ruptured during the second subevent. The stress is computed from 20 sec after the first subevent rupture time and every 10 sec. The maximum stress is reached (a) after about 65 sec for the stratified and (b) after about 60 sec for the homogeneous model, respectively.

ing between 5 and 15 km. Figure 5 emphasizes the depth dependence of Coulomb stress changes for a layered crustal structure. The presence of a low-velocity layer near the Earth surface modifies the stress pattern with respect to a homogeneous half-space. Within nearly 20 sec the negative stress pulse propagated along the fault plane. The highest stress amplitudes are reached after nearly 60 sec (peak value is about 0.17 MPa) for the stratified model and after 65 sec (peak value is 0.15 MPa) for the homogeneous crust. The difference between the arrival times of stress peaks for the two velocity structures considered in this article is well below the uncertainties in the origin time of the second subevent. The coincidence between the timing of peak stress on

the eastern edge of the fault plane and the nucleation of the second subevent, as resulting from the moment rate function (see Henry *et al.*, 2000) (Fig. 1b), suggests a nearly instantaneous triggering.

Discussion

It is widely accepted that faults interact with each other, promoting as well as inhibiting impending earthquakes. Fault interaction has been studied by looking at static stress changes calculated solving the elastostatic equation in homogeneous or stratified half-spaces (see Harris, 1998; Stein, 1999; King and Cocco, 2000, and references therein). Many

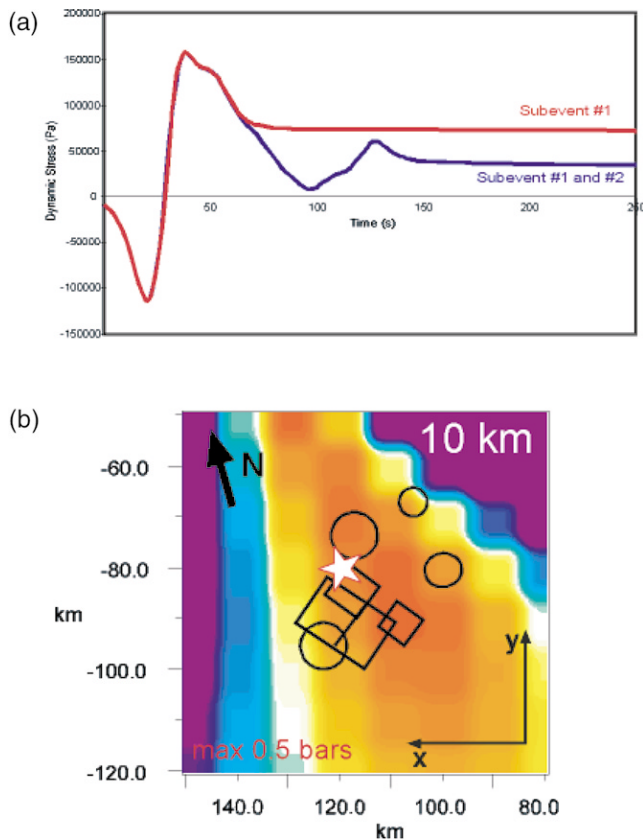


Figure 6. (a) Contribution to the stress time history resulting from the two subevents and computed at the grid point indicated by the star in the map below. (b) Static stress changes calculated for grid points inside the box b of Fig. 1. Relocated 1-week aftershocks are shown as circles, with the first 24 hours shown as diamonds.

applications have been focused on the analysis of aftershock locations and mechanisms (see Harris and Simpson, 1992; King *et al.*, 1994) and on seismicity-rate changes over longer time periods (see Reasenberg and Simpson, 1992; Stein, 1999, and references therein). Toda and Stein (2000) performed a similar modeling for the aftershocks of the 1998 Antarctic earthquake. We have calculated in the present study the dynamic stress changes caused by the main composite event in the area where most of the aftershocks are located (indicated by box b in Fig. 1b). We illustrate the results of our calculations in Figure 6, where we show the Coulomb stress changes calculated on fault planes having the same mechanism of the mainshock; we point out that the focal mechanisms of the five largest aftershocks are very similar to that of the main event (Toda and Stein, 2000). This figure confirms that aftershocks occurred in the area of static stress increase, in agreement with the results of Toda and Stein (2000). The static stress changes shown in Figure 6 represent the Coulomb stress perturbation 200 sec after the mainshock nucleation. In the same figure we also plot the time history of Coulomb stress changes (in a receiver point indicated by the star in the map) caused by either the com-

posite or the first subevent rupture. The static stress caused by the first rupture only is larger than the value caused by the composite event because the receiver point is in the stress shadow of the second subevent. This result emphasizes the importance of considering fault complexity and slip heterogeneity over large spatial scales in computing the induced stress field. Moreover, it also confirms that after a few minutes the dynamic induced stress reaches the static configuration, as also emphasized by Belardinelli *et al.* (1999) for the 1980 Irpinia earthquake. During the first 80 sec there is the simultaneous contribution of static and dynamic stress changes to the total induced stress field. For this particular application the dynamic stress amplitudes are larger than the static stress level. The problem of dynamic triggering has been investigated in recent years by different authors (e.g., Harris and Day, 1993; Gomberg *et al.*, 1997, 1998; Belardinelli *et al.* 1999; Kilb *et al.* 2000; Voisin *et al.*, 2000). Among these, Kilb *et al.* (2000) suggested that dynamic stress changes can trigger earthquakes not only at remote distances (see Hill *et al.*, 1993) but also in the near field. Our observations and modeling results support, for short-term interactions, the Kilb *et al.*, (2000) interpretation of earthquake dynamic triggering. Belardinelli *et al.* (2000) analyzed the response of a spring slider system to dynamic and static stress changes including inertia. They concluded that although static stress changes can hasten as well as delay impending failures, dynamic stress perturbations can only cause nearly instantaneous triggering. This means that a dynamic stress perturbation can promote a failure in a short time interval after the application of the induced load (a very short triggering delay). Following the results of Belardinelli *et al.* (2000), we have calculated the response of a spring slider system to an induced load represented by the stress time history shown in Figure 2, and we have found induced failures only as instantaneous triggering in correspondence of the arrival of the highest second dynamic stress peak. In other words, the spring slider response is always stable except when a nearly instantaneous failure occurs as the response to the positive dynamic stress pulse. Although the subjective choice of the constitutive and initial parameters makes this modeling attempt not general, it provides a numerical corroboration that dynamic stress changes induced from the first subevent can promote the triggering of the second subevent with a very short time delay.

Conclusions

We have computed the spatiotemporal evolution of stress changes caused by the first subevent of the great M_W 8.1 Antarctic earthquake of 25 March 1998. The stress time histories have been calculated using two different Earth models (listed in Table 1): the homogeneous model yields Coulomb stress that does not change with depth, whereas differences are present for the layered model (see Fig. 2). Because shear stress changes are greater than normal stress changes, our results do not depend on the adopted μ' value (Fig. 3). We mapped the temporal evolution of Coulomb

stress changes both on a horizontal layer (see Fig. 4) and on the second subevent fault plane (Fig. 5) for the two different Earth models here considered. The snapshots of induced Coulomb stress show that the highest stress increase in the area of the second subevent fault occurs between 55 and 65 sec at the fault edge closest to the first subevent depending on the assumed crustal structure. The value of the stress peak on the second subevent fault is 0.17 MPa for the stratified model. We must note, however, that since our calculations are bandlimited at high frequencies, this value can only represent a lower bound. Both the map view and the stress evolution on the second subevent fault plane shows positive and negative stress amplitudes depending on the different phases in the stress grams. It is evident, however, that there are persistent positive CFF amplitudes in the area surrounding the second subevent fault, before and after the passing of the negative stress pulse. The static stress level is reached after about 90 sec, and it is positive. The off-fault aftershocks lie in a region of positive static stress changes (see Fig. 6). The total stress perturbation in the aftershock area caused by the two subevents is lower than that generated by the first one alone. The difference between the arrival time of the second positive stress peak on the subevent fault plane and the inferred origin time lies within the uncertainties. Our interpretation of these modeling results suggests that the dynamic stress changes caused a nearly instantaneous triggering of the second subevent with a negligible delay. Moreover, our simulations support the conclusion that the fault constitutive laws are insensitive to negative stress pulses.

Acknowledgments

We thank Olivier Coutant, Fabrice Cotton, and Maria Elina Belardinelli for the availability of the code and for the collaborations in its optimization. We benefited from the useful discussions with Andrea Bizzarri and Maria Elina Belardinelli. We thank Ruth Harris and Joan Gomberg for reviewing the manuscript. Andrea Bizzarri also collaborated in performing the simulations with the spring-slider code. We thank Enzo Boschi for his encouragement and for supporting this research. Special thanks to Daniela Riposati who helped us draw some of the figures. This study was partially supported by the European Commission contract EVG1-1999-00001, Project Presap.

References

- Antolik, M., A. Kaverina, and D. Dreger (2000). Compound rupture of the great 1998 Antarctic plate earthquake, *J. Geophys. Res.* **105**, 23,825–23,838.
- Belardinelli, M. E., A. Bizzarri, and M. Cocco (2000). Earthquake triggering by static and dynamic stress changes, *Fall Meeting American Geophysical Union (AGU)*, San Francisco, December 2000.
- Belardinelli, M. E., M. Cocco, O. Coutant, and F. Cotton (1999). Redistribution of dynamic stress during coseismic ruptures: evidence for fault interaction and earthquake triggering, *J. Geophys. Res.* **104**, 14,925–14,945.
- Bouchon, M. (1981). A simple method to calculate Green's function for layered media, *Bull. Seism. Soc. Am.* **71**, 959–971.
- Cotton, F., and O. Coutant (1997). Dynamic stress variations due to shear faulting in a plane-layered medium, *Geophys. J. Int.* **128**, 676–688.
- Das, S., and K. Aki (1977). Fault plane with barriers: a versatile earthquake model, *J. Geophys. Res.* **82**, 5658–5670.
- Das, S., and C. Scholz (1981). Off-fault aftershock clusters caused by shear stress increase? *Bull. Seism. Soc. Am.* **71**, 1669–1675.
- Gomberg, J., M. L. Blanpied, and N. M. Beeler (1997). Transient triggering of near and distant earthquake, *Bull. Seism. Soc. Am.* **87**, 294–309.
- Gomberg, J., N. M. Beeler, M. L. Blanpied, and P. Bodin (1998). Earthquake triggering by transient and static deformation, *J. Geophys. Res.* **103**, 24,411–24,426.
- Harris, R. A. (1998). Introduction to special section: Stress triggers, stress shadows, and implications for seismic hazard, *J. Geophys. Res.* **103**, 24,347–24,358.
- Harris, R. A., and R. W. Simpson (1992). Changes in static stress on southern California faults after the 1992 Landers earthquake, *Nature* **360**, 251–254.
- Harris, R. A., and S. M. Day (1993). Dynamics of fault interaction: parallel strike slip faults, *J. Geophys. Res.* **98**, 4461–4472.
- Henry, C., S. Das, and J. H. Woodhouse (2000). The great March 25, 1998, antarctic Plate earthquake: moment tensor and rupture history, *J. Geophys. Res.* **105**, 16,097–16,118.
- Hill, D. P., P. A. Reasenberg, A. Michael, W. J. Arabaz, G. Beroza, D. Brumbaugh, J. N. Brune, R. Castro, S. Davis, D. dePollo, W. L. Ellsworth, et al. (1993). Seismicity remotely triggered by the magnitude 7.3 Landers, California, earthquake, *Science* **260**, 1617–1623.
- Kennet, B. L., and N. J. Kerry (1979). Seismic wave in a stratified half space, *Geophys. J. R. Astr. Soc.* **84**, 557–583.
- Kilb, D., J. Gomberg, and P. Bodin (2000). Triggering of earthquake aftershocks by dynamic stresses, *Nature* **408**, 570–574.
- King, G. C. P., and M. Cocco (2000). Fault interaction by elastic stress changes: new clues from earthquake sequences, *Adv. Geophys.* **44**, 1–38.
- King, G. C. P., R. S. Stein, and J. Lin (1994). Static stress changes and the triggering of earthquakes, *Bull. Seism. Soc. Am.* **84**, 935–953.
- Mooney, W. D., G. Laske, and T. G. Masters (1998). Crust 5.1: a global crustal model at $5^\circ \times 5^\circ$, *J. Geophys. Res.* **103**, 727–747.
- Nettles M., T. C. Wallace, and S. Beck (1999). The March 25, 1998 Antarctic plate earthquake, *Geophys. Res. Lett.* **26**, 2097–2100.
- Okada, Y. (1992). Internal deformation due to shear and tensile faults in a half-space, *Bull. Seism. Soc. Am.* **82**, 1018–1040.
- Reasenberg, P. A., and R. W. Simpson (1992). Response of regional seismicity to the static stress change produced by the Loma Prieta earthquake, *Science* **255**, 1687–1690.
- Rybicki, K. (1973). Analysis of aftershocks on the basis of dislocation theory, *Phys. Earth Planet. Interiors* **7**, 409–422.
- Simpson, R. W., and P. A. Reasenberg (1994). Earthquake-induced static stress changes on central California faults, *U. S. Geol. Surv. Profess. Pap.* 1550-F, F55–F89.
- Stein, R. S., G. C. P. King, and J. Lin (1992). Change in failure stress on the southern S. Andreas fault system caused by the 1992 magnitude = 7.4 Landers earthquake, *Science* **258**, 1328–1332.
- Stein, R. S. (1999). Stress transfer in earthquake occurrence, *Nature* **402**, December.
- Toda, S., and R. S. Stein (2000). Did stress triggering cause the large off-fault aftershocks of the March 1998 $M_w = 8.1$ Antarctic plate earthquake? *Geophys. Res. Lett.* **27**, 2301–2304.
- Voisin, C., M. Campillo, I. R. Ionescu, F. Cotton, and O. Scotti (2000). Dynamic versus static stress triggering and friction parameters: inference from the November 23, 1980, Irpinia earthquake, *J. Geophys. Res.* **105**, 21,647–21,659.

Istituto Nazionale di Geofisica e Vulcanologia
Rome, Italy
(A.A., M.C.)

Department of Earth Science
University of Oxford
Oxford, U. K.
(S.D., C.H.)